Lawrence Berkeley National Laboratory

Recent Work

Title

Search for C ii emission on cosmological scales at redshift Z ~ 2.6

Permalink

https://escholarship.org/uc/item/7k37s81n

Journal

Monthly Notices of the Royal Astronomical Society, 478(2)

ISSN

0035-8711

Authors

Pullen, Anthony R
Serra, Paolo
Chang, Tzu-Ching
et al.

Publication Date

2018-08-01

DOI

10.1093/mnras/sty1243

Peer reviewed

eScholarship.org Powered by the California Digital Library
University of California

Monthly Notices
of the
ROYAL ASTRONOMICAL SOCIETY

MNRAS **478,** 1911–1924 (2018)
Advance Access publication 2018 May 14

doi:10.1093/mnras/sty1243

Search for C II emission on cosmological scales at redshift $Z \sim 2.6$

Anthony R. Pullen,[1,2★] Paolo Serra,[3,4] Tzu-Ching Chang,[3,4,5] Olivier Doré[3,4] and Shirley Ho[2,6]

[1]*Center for Cosmology and Particle Physics, Department of Physics, New York University, 726 Broadway, New York, NY, 10003, USA*
[2]*McWilliams Center for Cosmology, Department of Physics, Carnegie Mellon University, 5000 Forbes Ave, Pittsburgh, PA, 15213, USA*
[3]*Jet Propulsion Laboratory, California Institute of Technology, Pasadena, CA 91109, USA*
[4]*California Institute of Technology, Pasadena, CA 91125, USA*
[5]*Academia Sinica Institute of Astronomy and Astrophysics, PO Box 23-141, Taipei 10617, Taiwan*
[6]*Lawrence Berkeley National Laboratory, 1 Cyclotron Road, Berkeley, CA 94720, USA*

Accepted 2018 May 4. Received 2018 April 27; in original form 2017 August 9

ABSTRACT

We present a search for C II emission over cosmological scales at high redshifts. The CII line is a prime candidate to be a tracer of star formation over large-scale structure since it is one of the brightest emission lines from galaxies. Redshifted C II emission appears in the submillimeter regime, which means it could potentially be present in the higher frequency intensity data from the *Planck* satellite is used to measure the cosmic infrared background (CIB). We search for CII emission over redshifts $z = 2-3.2$ in the *Planck* 545 GHz intensity map by cross-correlating the three highest frequency *Planck* maps with spectroscopic quasars and CMASS galaxies from the Sloan Digital Sky Survey III, which we then use to jointly fit CII intensity, CIB parameters, and thermal Sunyaev–Zeldovich (SZ) emission. We report a measurement of an anomalous emission $I_\nu = 6.6^{+5.0}_{-4.8} \times 10^4$ Jy sr^{-1} at 95 per cent confidence, which could be explained by C II emission, favouring collisional excitation models of C II emission that tend to be more optimistic than models based on C II luminosity scaling relations from local measurements; however, a comparison of Bayesian information criteria reveals that this model and the CIB & SZ model are equally plausible. Thus, more sensitive measurements will be needed to confirm the existence of a large-scale CII emission at high redshifts. Finally, we forecast that intensity maps from Planck cross-correlated with quasars from the Dark Energy Spectroscopic Instrument would increase our sensitivity to CII emission by a factor of 5, while the proposed Primordial Inflation Explorer could increase the sensitivity further.

Key words: ISM: molecules – galaxies: high-redshift – large-scale structure of the universe – cosmology: observations – cosmology: theory – submillimeter: ISM.

1 INTRODUCTION

Galaxy spectroscopy is one of the most vital tools in astronomy, providing information over a wide range of scales from the nature of our local neighbourhood of galaxies to the evolution of the Universe. One spectral line that has been studied over the years in this field is the fine-structure line from ionized carbon, or C II. Carbon, which is very abundant due to its production in stars, has an ionization energy of 11.26 eV, allowing it to be more easily ionized than hydrogen. At gas temperatures greater than 91K, C II is excited through the energy transition $^2P_{3/2} \rightarrow {}^2P_{1/2}$, which produces an emission line at 157.7 μm that we will refer to as CII. The C II line is an effective tracer of star formation, in that it tends to be the brightest line in the spectra of star-forming galaxies, contributing 0.1–1 per cent of the far-infrared luminosity in low-redshift galaxies. It is also well known that the bulk of this emission tends to come from photo-dissociation regions (PDRs). CII has been detected in star-forming local galaxies for decades, while current instruments such as the Atacama Large Microwave/Submillimeter Array have begun to extend detections out to high-redshift CII galaxies, including one C II galaxy at $z \sim 7$ (Maiolino et al. 2015) within the epoch of reionization (EoR) when early star formation reionized the intergalactic medium. These instances of success show the potential of CII emission to reveal much about our local Universe.

However, the C II galaxies that are detected individually at a high angular resolution have been shown to be the only brightest and most massive of all CII-emitting galaxies, characterized by a steep faint-end slope in the UV luminosity function (Bouwens et al. 2015), which means the more representative low-mass galaxies are out of

★ E-mail: anthony.pullen@nyu.edu

© 2018 The Author(s)
Published by Oxford University Press on behalf of the Royal Astronomical Society

Downloaded from https://academic.oup.com/mnras/article-abstract/478/2/1911/4995923 by Lawrence Berkeley National Laboratory user on 22 January 2019

reach for these surveys. In addition, even the most powerful upcoming survey telescopes will not produce large-scale galaxy samples past redshift $z=4$, thereby limiting the redshifts and scales usable for cosmology. These concerns could be rectified by producing maps of line emission at a low angular resolution, a technique called intensity mapping (IM) (Scott & Rees 1990; Madau, Meiksin & Rees 1997; Suginohara, Suginohara & Spergel 1999; Chang et al. 2008; Wyithe, Loeb & Geil 2008). Capturing the aggregate emission of all emitters gives us a representative picture of the properties of galaxies and star-forming regions, while also allowing us to observe directly the largest cosmological scales (>1 Gpc) of large-scale structure (LSS), the EoR, and the potentially preceding 'dark ages'. The IM method has been well developed in the literature, and it has traditionally been considered in the context of mapping the 21-cm line from neutral hydrogen. There has been a proliferation of 21-cm survey efforts, with the Canadian HI Mapping Experiment (Bandura et al. 2014), the Hydrogen Epoch of Reionization Array (DeBoer et al. 2017), and the Square Kilometre Array (Santos et al. 2015) as the upcoming benchmarks for this effort. Lately, there has been great interest in mapping other bright lines, including C II (Basu, Hernández-Monteagudo & Sunyaev 2004; Gong et al. 2012; Silva et al. 2015; Yue et al. 2015), CO (Righi, Hernández-Monteagudo & Sunyaev 2008; Carilli 2011; Lidz et al. 2011; Pullen et al. 2013; Breysse, Kovetz & Kamionkowski 2014; Mashian, Sternberg & Loeb 2015; Li et al. 2016), Lyα (Silva et al. 2013; Pullen, Doré & Bock 2014; Gong et al. 2014; Comaschi & Ferrara 2016), and Hα (Gong et al. 2017; Silva et al. 2017). A few surveys are also being considered to map other lines and are at various stages of development, including the CO Mapping Pathfinder (Li et al. 2016), TIME (C II) (Crites et al. 2014), CONCERTO (C II) (Serra, Doré & Lagache 2016), HETDEX (Lyα) (Hill et al. 2008), SPHEREx (Hα, O III, Lyα) (Doré et al. 2014), and CDIM (Hα, O III, Lyα) (Cooray et al. 2016). The consideration of alternatives to the 21-cm line for IM has been greatly boosted by the recent detection of CO correlations in LSS through the COPPS survey (Keating et al. 2016).

While IM studies are usually considered in terms of measuring autocorrelations, cross-correlating an intensity map (Visbal & Loeb 2010) with another tracer of LSS has advantages in that (1) instrumental noise bias is eliminated, making accessible small-scale modes that are more numerous than the large-scale modes, and (2) other lines from different redshifts in the IM map will not correlate with the other LSS tracer. In future, we expect to cross-correlate intensity maps from different line tracers at the same redshift (Lidz et al. 2011; Gong et al. 2012; Silva et al. 2013; Gong et al. 2014; Chang et al. 2015), e.g. C II and 21-cm lines, in order to track how different LSS phases are correlated. Even now, cross-correlations have been performed between diffuse emission maps and low-redshift LSS tracers to detect the particular diffuse emission at a given redshift, including the current 21-cm detections (Chang et al. 2010; Masui et al. 2013). Previously, Pullen et al. (2013) performed a cross-correlation between the Wilkinson Microwave Anisotropy Probe temperature maps and a photometric quasar sample from the Sloan Digital Sky Survey (SDSS) II, allowing us to place limits on large-scale CO emission. We predicted that *Planck* could potentially detect C II emission that is ∼1000 times brighter than CO emission. Also, while contamination of CII maps by thermal dust (Planck Collaboration et al. 2014a) and, to a much less extent, CO emission (Lidz & Taylor 2016; Cheng et al. 2016) is a concern, thermal dust and CO contamination in a cross-correlation will only increase the noise without biasing the result.

In this paper, we measure the intensity of C II diffuse emission by performing a Monte Carlo Markov Chain (MCMC) analysis fitting for CII and cosmic infrared background (CIB) emission jointly using cross-correlations between high-frequency intensity maps with LSS tracers. Specifically, we measure angular cross-power spectra of overdensity maps of both spectroscopic quasars at redshift $z = 2.6$ and CMASS galaxies at redshift $z = 0.57$ from the SDSS-III Baryon Oscillations Spectroscopic Survey (BOSS) (Eisenstein et al. 2011) with the {353, 545, 857} GHz intensity maps from the *Planck* satellite (Lamarre et al. 2010; Planck HFI Core Team et al. 2011) to fit jointly for the C II intensity and three CIB parameters. The spectroscopic quasars are limited to redshifts $z= 2-3.2$, which comprise the redshift range of CII emission within the 545 GHz band, while the redshifts of the CMASS galaxies are too low to correlate with C II emission in the Planck maps. Thus, we expect the C II emission to appear only in the cross-correlation of the quasars with the 545 GHz Planck map, while the other five cross-correlations are used to fit the CIB parameters.

We confirm that the MCMC analysis' best-fitting model for the CIB and CII emission constitutes a good fit to the data, with the CIB parameters in broad agreement with previous CIB analyses, and a favoured value for the C II intensity at $z = 2.6$ of $I_{\rm C\,II} = 6.6^{+5.0}_{-4.8} \times 10^4$ Jy sr^{-1} (95 per cent confidence level) for the CII emission. Although this is not quite a detection, it does support the possibility that the high-redshift CII emission is present alongside the continuum CIB emission. Note that the favoured value of $I_{\rm C\,II}$ is consistent with C II emission models from Gong et al. (2012) and Silva et al. (2015) that are constructed from collisional excitation models, and is in tension with lower emission models constructed from luminosity scaling relations based on local measurements. It is possible that other extragalactic emission lines could contribute to this emission; based on local measurements, we expect ∼3 per cent of the excess cross-correlation of the Planck 545 GHz band with quasars and not due to CIB that is comprised of interloping lines based on local line ratio measurements. Using Bayesian evidence ratio, or Bayes Factor, we find that both this model and the non-CII models are equally favoured, and more sensitive data will be needed to confirm or rule out high-redshift CII emission. Finally, we forecast what the sensitivity of this measurement would be for upcoming surveys. Replacing BOSS quasars and CMASS galaxies with luminous red galaxies (LRGs) and quasars from the upcoming Dark Energy Spectroscopic Instrument (DESI) (Levi et al. 2013) could increase the signal-to-noise ratio (SNR) to 10. Further replacing Planck with the proposed Primordial Inflation Explorer (PIXIE) (Kogut et al. 2011) could increase the SNR to 26, in addition to allowing isolation of CII emission from nearby lines due to PIXIE's high spectral resolution.

The paper is as follows: in Section 2 we describe the *Planck* and SDSS data products we use. In Section 3, we present the estimator for the intensity-LSS angular cross-power spectra, and we present our cross-power spectrum measurements and checks for systematic effects in Section 4. In Section 5, we place constraints on C II emission using MCMC analysis, and in Section 6 we discuss how our C II constraints compare with various C II models and what this implies for upcoming C II surveys. We conclude in Section 7.

2 DATA

2.1 Planck Maps

We use data from the *Planck* satellite that measured the intensity and polarization of the cosmic background radiation (CBR) over the entire sky. The CBR was observed during the time period of August 2009 and August 2013 using a 74-detector array consisting of two

Downloaded from https://academic.oup.com/mnras/article-abstract/478/2/1911/4995923 by Lawrence Berkeley National Laboratory user on 22 January 2019

instruments. The Low-Frequency Instrument (Bersanelli et al. 2010; Mennella et al. 2011) implements pseudo-correlation radiometers to observe three frequency channels at 30, 40, and 70 GHz. The High-Frequency Instrument (Lamarre et al. 2010; Planck HFI Core Team et al. 2011) uses bolometers and observes six frequency channels at 100, 143, 217, 353, 545, and 857 GHz.

We use the 545 GHz intensity map to trace the redshifted C II intensity over the sky, while additionally using the 353 and 857 GHz maps to constrain the CIB and SZ emission and clustering. The maps have beam full-widths at half-maximum of the order of a few arcmin. These maps, like all *Planck* maps, use HEALPIX (Górski et al. 2005) pixelization with $N_{\rm side} = 2048$. Superimposed on these maps are one common mask constructed to remove pixels with bright Galactic emission and point sources. Our point source veto mask is a union of all the point source veto masks for all three maps. The *Planck* Galactic emission mask with 2° apodization leaves 33.8 per cent of the sky, while our combined *Planck* point source mask with 0.5° apodization leaves on its own 94.5 per cent of the sky. Together, these two masks combined leave 33.2 per cent of the sky in the survey, comprising the high- and low-latitude regions near the Galactic poles. Note that we also use the 545 GHz bandpass filter to construct a radial selection function we use to predict the CII emission angular power spectrum (see Fig. 5).

For the unmasked regions, we still expect emission from the cosmic microwave background including SZ perturbations, the CIB, and thermal dust along with the potential CII emission. We do not attempt to subtract these extra sources of emission directly. Instead we rely on our use of cross-correlations with LSS tracers to remove the base CMB and thermal dust perturbations from our C II estimator, while fitting for SZ and CIB emission simultaneously with C II emission. However, we do expect all these extra sources of emission to contribute to the parameter errors.

2.2 Boss maps

SDSS-III (Eisenstein et al. 2011), similar to SDSS I and II (York et al. 2000), is constructed from galaxies and point sources detected by a 2.5-m telescope (Gunn et al. 2006) with a mounted imaging camera (Gunn et al. 1998) with five filters (*ugriz*) (Fukugita et al. 1996; Smith et al. 2002; Doi et al. 2010) that images over one-third of the sky. Astrometric calibration (Pier et al. 2003), photometric reduction (Lupton et al. 2001), and photometric calibration (Padmanabhan et al. 2008) are performed by automated pipelines. Bright galaxies, LRGs, and quasars are selected for follow-up spectroscopy (Eisenstein et al. 2001; Strauss et al. 2002; Richards et al. 2002; Blanton et al. 2003; Smee et al. 2013). This survey took place between 1998 August and 2013 May. The SDSS-III specifically tasked the BOSS (Dawson et al. 2013) with constructing a spatially uniform low-redshift galaxy sample and a sample of high-redshift quasars, primarily to constrain dark energy.

In our analysis we use the BOSS spectroscopic quasar sample (Pâris et al., in preparation) from Data Release 12 (DR12) (Alam et al. 2015) to trace LSS at $z = 2.6$. The quasars were targeted under a CORE+BONUS sample (Ross et al. 2012), where the CORE quasars are uniformly sampled for clustering studies and the BONUS quasars are not and mainly used to sample the Lyα forest. We use only the CORE quasars in our analysis. The target selection for the CORE quasars was implemented by applying the extreme deconvolution (XD) technique, which determines the distribution points in parameter space, to quasars and stars in colour space in order to separate their populations (XDQSO) (Bovy et al. 2011). The spectra of the targeted point sources are then visually analysed to determine their spectroscopic redshifts. A mask comprising the BOSS imaging regions is also constructed, with veto masks applied to remove areas near bright stars, centreposts of the spectroscopic plates, regions with bad photometry, particularly *u* band data, and regions where less than 75 per cent of CORE targets received a BOSS spectroscopic fibre (White et al. 2011). This method has been used and is explained in more detail in previous SDSS quasar analyses (White et al. 2012; Pâris et al. 2014; Eftekharzadeh et al. 2015), and is currently being used for the Extended BOSS (eBOSS) quasar target selection (Myers et al. 2015). We implement this procedure on point sources from DR12, giving us a catalogue of 178 622 quasars. We then keep the ones in the redshift range $z = 2-3.2$ in pixels with mask weight greater than 90 per cent, leaving us with 82 522 quasars over 8294 deg^2, with an overlap with the *Planck* map of 6483 deg^2 with 75 244 quasars.

We also use the CMASS spectroscopic galaxy sample from BOSS DR12 (Alam et al. 2015; Alam et al. 2016; Reid et al. 2016) that was publicly released with the final BOSS data set. This galaxy sample does not correlate with CII emission; we use it to constrain the CIB and SZ emission and clustering. The full CMASS sample (Alam et al. 2015) contains 862 735 galaxies over an area of 9376 deg^2 with a mean redshift of 0.57 and is designed to be stellar-mass-limited at $z > 0.45$. Each spectroscopic sector, or region covered by a unique set of spectroscopic tiles (Aihara et al. 2011), was constructed to have an overall completeness, or a fraction of spectroscopic targets observed, over 70 per cent and a redshift completeness, or a fraction of observed galaxies with quality spectra, over 80 per cent. We take the full CMASS sample and remove galaxies outside the redshift range $z = 0.43-0.7$ and galaxies within pixels with coverage less than 90 per cent, leaving us with 777 202 galaxies over an area of 10 229 deg^2.

For both the quasars and galaxies, we construct overdensity maps $\delta_i = (n_i - \bar{n})/\bar{n}$, where i is the sky pixel. For the quasars, n_i is the actual number of quasars in pixel i, while for galaxies n is the weighted number of galaxies $n_i = \sum_{j \in \text{pixel}\, i} w_j$ where w_j is the systematic weight (Anderson et al. 2014) of galaxy j. The map is given as a HEALPIX pixelization with $N_{\rm side} = 1024$. We do not attempt to weight the sky pixels by their observed areas; the HEALPIX pixels are much smaller than the observed sectors that define the completeness, and the weighting individual pixels could introduce extra power due to possible errors in the completeness on small scales. Finally we perform a 0.5° apodization on both quasar and CMASS galaxy masks.

3 CROSS-CORRELATION ANALYSIS

We construct six angular cross-power spectra C_ℓ, cross-correlating the 353, 545, and 857 GHz Planck maps with our BOSS quasar and CMASS galaxy samples. Specifically, we estimate each angular cross-power spectrum in nine band powers of uniform width, where we use the convention introduced in Hivon et al. (2002)

$$\tilde{C}_b = \sum_\ell P_{b\ell} C_\ell$$
$$C_\ell = Q_{\ell b} \tilde{C}_b, \quad (1)$$

where

$$P_{b\ell} = \begin{cases} \frac{\ell(\ell+1)}{2\pi\Delta b} & \text{if } \ell \in \text{b}; \\ 0 & \text{otherwise.} \end{cases}, \quad (2)$$

Downloaded from https://academic.oup.com/mnras/article-abstract/478/2/1911/4995923 by Lawrence Berkeley National Laboratory user on 22 January 2019

and

$$Q_{\ell b} = \begin{cases} \frac{2\pi}{\ell(\ell+1)} & \text{if } \ell \in \text{b;} \\ 0 & \text{otherwise.} \end{cases}, \tag{3}$$

where Δb is the bin size. We consider multipoles in the range $100 \leq \ell \leq 1000$, which for the quasars at redshift $z = 2.6$ that correlate with the C II emission in the 545 GHz band corresponds to transverse scales $k_\perp = 0.023-0.23$ h Mpc^{-1}. This range allows us to avoid CMB-quasar correlations from the integrated Sachs–Wolfe effect (Sachs & Wolfe 1967) and cosmic variance on large scales as well as non-linear clustering on small scales. However, non-linear clustering should appear in this ℓ-range for the CMASS galaxies, so we also consider in this analysis how these non-linear scales affect our CII constraints.

We estimate $\tilde{C}_b^{TL}$ between Planck map T and LSS tracer map L in band b using a pseudo-C_ℓ estimator of the form (Hivon et al. 2002; Tristram et al. 2005)

$$\hat{C}_b^{TL} = \frac{2\pi}{b(b+1)} \sum_{b'} [\mathcal{M}^{-1}]_{bb'}^{TL} \tilde{D}_{b'}^{TL}, \tag{4}$$

where $\tilde{D}_b^{TL} = \sum_\ell P_{b\ell} \hat{D}_\ell^{TL}$ is the angular cross-power spectrum of the masked maps, given by

$$\hat{D}_\ell^{TL} = \frac{1}{2\ell+1} \sum_{m=-\ell}^{\ell} a_{\ell m}^T a_{\ell m}^{L*}, \tag{5}$$

where $a_{\ell m}^T$ and $a_{\ell m}^L$ are the spherical harmonic transforms of the maps with the masked pixels set to zero. The matrix $\mathcal{M}_{bb'}^{TL}$ is given by

$$\mathcal{M}_{bb'}^{TL} = \sum_{\ell\ell'} P_{b\ell} M_{\ell\ell'}^{TL} E_{\ell'}^T E_{\ell'}^L Q_{\ell' b'}, \tag{6}$$

where $E_\ell^T = p_\ell^T B_\ell^T$ and $E_\ell^L = p_\ell^L$, p_ℓ and B_ℓ are the pixel and beam window functions, respectively, and $M_{\ell\ell'}^{TL}$ is the mode-mode coupling matrix resulting from partial sky coverage. This matrix is given by

$$M_{\ell\ell'}^{TL} = \frac{2\ell'+1}{4\pi} \sum_{\ell''} (2\ell''+1) W_{\ell''}^{TL} \begin{pmatrix} \ell & \ell' & \ell'' \\ 0 & 0 & 0 \end{pmatrix}^2, \tag{7}$$

where

$$W_\ell^{TL} = \frac{1}{2\ell+1} \sum_{m=-\ell}^{\ell} w_{\ell m}^T w_{\ell m}^{L*}, \tag{8}$$

the angular cross-power spectrum of the two masks.

We analytically compute the covariance matrix using the formulas from Tristram et al. (2005), modified to account for band powers as

$$\begin{aligned} Cov &\left[\hat{C}_b^{T_1L_1}, \hat{C}_{b'}^{T_2L_2}\right] \\ &= \frac{(2\pi)^2}{b(b+1)b'(b'+1)} \sum_{b_1 b_2 \ell_1 \ell_2} [\mathcal{M}^{-1}]_{bb_1}^{T_1L_1} [\mathcal{M}^{-1}]_{b'b_2}^{T_2L_2} P_{b_1\ell_1} P_{b_2\ell_2} \\ &\times \left[\frac{\mathcal{M}_{\ell_1\ell_2}^{(2)}(W^{T_1T_2,L_1L_2}) C_{\ell_1}^{T_1T_2} C_{\ell_2}^{L_1L_1} \delta_{L_1L_2}}{2\ell_2+1} \right. \\ &\left. + \frac{\mathcal{M}_{\ell_1\ell_2}^{(2)}(W^{T_1L_2,T_2L_1}) C_{\ell_1}^{T_1L_2} C_{\ell_2}^{T_2L_1}}{2\ell_2+1} \right] \end{aligned} \tag{9}$$

where we use C_ℓs measured from the data to compute the covariance, we assume that the set of LSS tracers are from different redshifts and thus uncorrelated, and the expressions for $\mathcal{M}_{\ell_1\ell_2}^{(2)}$ are given in equation27 of Tristram et al. (2005). This expression for the covariance is actually not symmetric; the asymmetry is due to the following approximation used in the derivation (see equation A9 in the appendix of Tristram et al. (2005))

$$\begin{aligned} \sum_{\ell_1 m_1} & C_{\ell_1}^{XY} \; E_{\ell_1}^X E_{\ell_1}^Y K_{\ell m \ell_1 m_1}^X K_{\ell' m' \ell_1 m_1}^{Y*} \\ &\simeq C_\ell^{XY} E_\ell^X E_\ell^Y \sum_{\ell_1 m_1} K_{\ell m \ell_1 m_1}^X K_{\ell' m' \ell_1 m_1}^{Y*}. \end{aligned} \tag{10}$$

Instead, the approximation should be agnostic with respect to ℓ and ℓ', so, following the treatment in Brown, Castro & Taylor (2005), we make the replacement

$$C_{\ell_{1,2}}^{XY} E_{\ell_{1,2}}^X E_{\ell_{1,2}}^Y \rightarrow \sqrt{C_{\ell_1}^{XY} E_{\ell_1}^X E_{\ell_1}^Y C_{\ell_2}^{XY} E_{\ell_2}^X E_{\ell_2}^Y}, \tag{11}$$

for every C_ℓ in equation (9). Note that $C_\ell^{T_1T_2}$ includes contributions from the CIB, CMB, and thermal dust, as well as instrumental noise if $T_1 = T_2$, and C_ℓ^{LL} includes shot noise.

4 RESULTS

We present in Fig. 1 our estimates of the angular cross-power spectra between the three Planck bands and both the quasar and CMASS galaxy samples, along with statistical errors. The C_ℓs are detected with high significance, and we are able to fit them well with a sum of the CIB halo model from Planck Collaboration et al. (2014c) and Shang et al. (2012), and an excess due to CII emission (see Section 5). Note that the C_ℓs for the Planck-galaxy cross-correlations agree with those presented in Serra et al. (2014). However, these C_ℓs are a bit higher than the model at small scales, which may be due to non-linear clustering. We test the significance of these C_ℓs by removing the three highest ℓ-bins ($\ell > 700$) of the three Planck-galaxy C_ℓs from our model fits, finding that the model does not change significantly (see Section 5).

4.1 Rotation test

We test our estimator by cross-correlating the Planck maps with LSS tracer maps rotated azimuthally $\phi \rightarrow \phi + 90^\circ$. The result, shown in Fig. 2, has $\chi^2 < 2.5$ ($N_{\rm dof} = 9$) for all the cross-power spectra, consistent with a null result.

4.2 Mask test

Residual foregrounds from the Galaxy such as thermal dust and bright point sources could be correlated with systematic errors in our quasar and galaxy samples, contaminating our cross-correlations. Since residual foregrounds are not statistically isotropic, we would expect our measurement to be dependent on the survey area if it were heavily contaminated. In order to test this, we repeat our power spectrum measurement, replacing the 40 per cent Galactic mask with the 20 per cent Planck Galactic mask. We then estimate the difference between our fiducial estimate (40 per cent Galactic mask) with the 20 per cent mask, which we show in Fig. 3. It appears that the estimate using the alternate mask is consistent with the fiducial estimate, with $\chi^2 < 1.5$ ($N_{\rm dof} = 9$) for all the cross-power spectra, showing that our power spectrum measurement is converged with regard to the masking area.

Downloaded from https://academic.oup.com/mnras/article-abstract/478/2/1911/4995923 by Lawrence Berkeley National Laboratory user on 22 January 2019

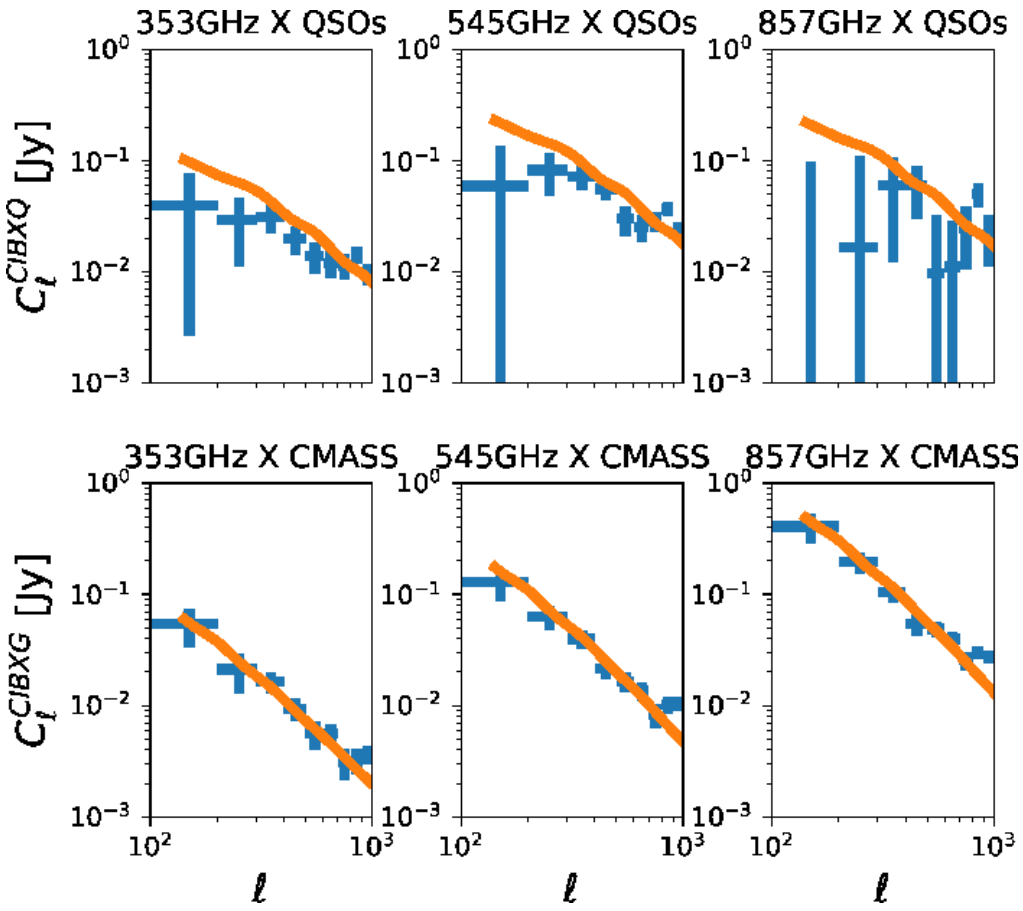

Figure 1. Estimates of the six cross-power spectra from the best-fitting parameters in our model, together with the measurements, obtained cross-correlating Planck CIB maps at 353, 545, and 857 GHz with LRGs and quasars (QSOs). The excesses in the Planck-LRG cross-correlations at high ℓ may be due to non-linear clustering, though we later show that these scales do not significantly affect our results.

4.3 Jackknife test

We also test for foregrounds by performing jackknife tests, shown in Fig. 4. For the Planck-quasar (Planck-CMASS) power spectra, we divide both maps into 40 (37) regions, which allow us to construct multiple estimates of C_ℓ^{T-Q} (C_ℓ^{T-G}), excluding each jackknife region. This test checks that our C_ℓ results are not biased by foregrounds in a particular region. For both tracers, the spread of the estimates are well within the errors, suggesting that our C_ℓ measurements do not vary across the sky and that foregrounds are not dominating our signal.

5 CII CONSTRAINTS

In order to constrain the mean amplitude of the C II signal from CIB galaxies, we fit six angular cross-power spectra obtained by cross-correlating three Planck brightness temperature, i.e. intensity maps (at 353, 545, and 857 GHz) with both the QSO overdensity map at $z\sim$ 2.2, and the LRG map at $z \sim 0.5$. Given the rest-frame wavelength of the C II emission line at 157.7 μm, and the redshift kernels of the LSS tracers, the only observable containing the CII line is the cross-correlation measurement between QSOs and the Planck temperature map at 545 GHz. All other cross-power spectra are used to constrain both the emission and clustering of CIB sources in the context of the halo model (Shang et al. 2012; Planck Collaboration et al. 2014c). In this regard, we note that, while in principle it is possible to use measurements of the CIB autopower spectra to constrain the main parameters of the model, this kind of analysis is complicated by the need to include many free parameters to account for the shot-noise power spectra of CIB anisotropies at the frequencies of interest. In order to keep our analysis as simple as possible, we include the information encapsulated in the CIB autopower spectra simply as priors on the main parameters of our model of CIB galaxies.

5.1 Cross-power spectra and the CIB model

The amount of correlation between a temperature map and a generic LSS map (in our case a galaxy or a quasar map) is quantified by their cross-power spectrum that can be expressed as:

$$C_\ell^{\mathrm{LSS-T}} = \int \frac{\mathrm{d}z}{\chi^2}\left(\frac{\mathrm{d}\chi}{\mathrm{d}z}\right)^{-1} b_{\mathrm{LSS}} b_{\mathrm{CIB}}(k,z) \frac{\mathrm{d}N}{\mathrm{d}z}(z)\frac{\mathrm{d}S}{\mathrm{d}z}(z,\nu)P_{\mathrm{DM}}(k,z), \quad (12)$$

where $k = \ell/\chi(z)$. The bias b_{LSS} for LRGs is equal to $b_{\mathrm{LRG}} = 2.1$ (Alam et al. 2017). The BOSS quasar bias b_{QSO} has been measured in White et al. (2012) to be in the range $b_{\mathrm{QSO}} = 3.6-4.3$. We perform our own fit for b_{QSO} by measuring the angular autopower

Downloaded from https://academic.oup.com/mnras/article-abstract/478/2/1911/4995923 by Lawrence Berkeley National Laboratory user on 22 January 2019

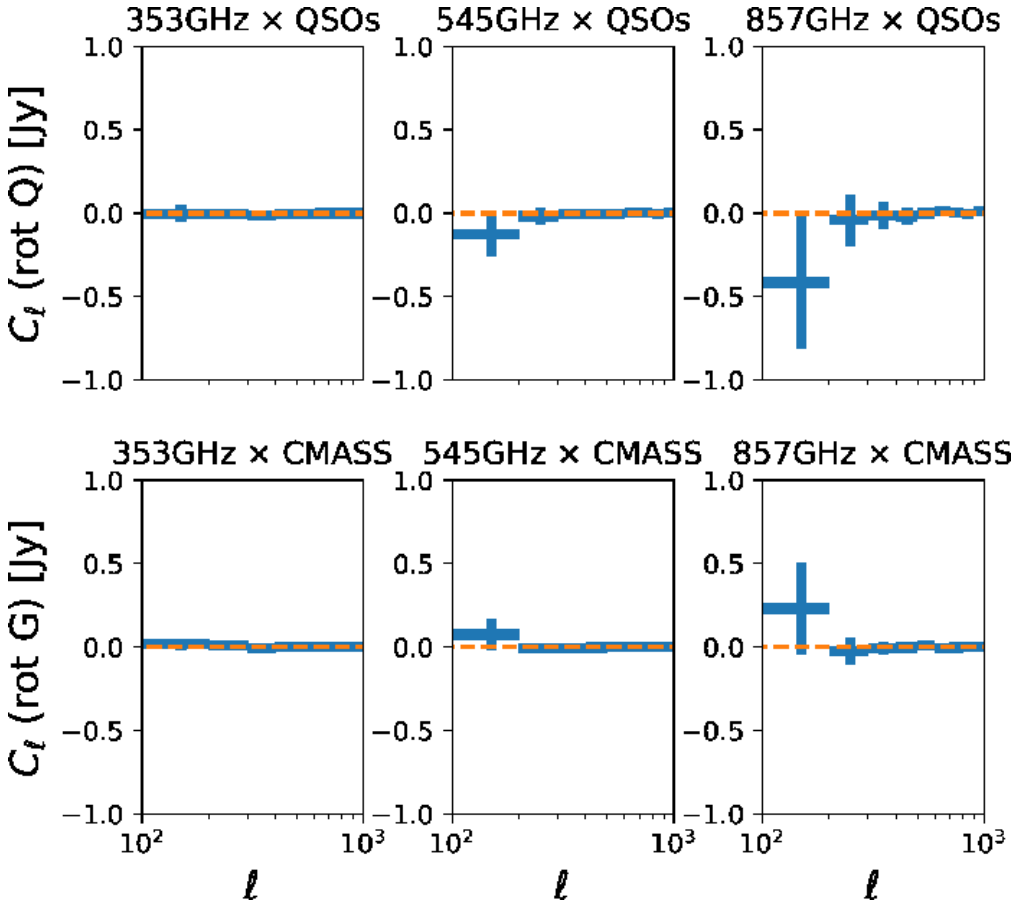

Figure 2. The Planck-quasar (top) and Planck-CMASS (bottom) angular cross-power spectra with the quasar and CMASS maps rotated by 90°. The spectra appear to be consistent with a null result.

spectrum using a quadratic maximum-likelihood estimator (Hirata et al. 2004; Pullen & Hirata 2013), finding $b_{\rm QSO}= 3.5 \pm 0.3$. The redshift distributions for both LRGs and QSOs were computed from the tracer redshift catalogues and are shown in Fig. 5.

The dark matter power spectrum $P_{\rm DM}(k, z)$ is computed using CAMB (Lewis, Challinor & Lasenby 2000) assuming best-fitting parameters from Planck Collaboration et al. (2016). Both bias $b_{\rm CIB}(k, z)$ and the redshift distribution $\frac{{\rm d}S}{{\rm d}z}(z, \nu)$ of CIB sources can be computed using a halo model for CIB anisotropies introduced in Planck Collaboration et al. (2014c) and Shang et al. (2012), and successfully applied in many subsequent analyses, including Viero et al. (2013), Planck Collaboration et al. (2014c), and Serra et al. (2014, 2016).

In the following, we will briefly discuss the main parameters used in the analysis, and refer the reader to the aforementioned papers for an exhaustive description of the model. The redshift distribution of CIB sources at the observed frequency ν can be written as:

$$\frac{{\rm d}S_\nu}{{\rm d}z} = \frac{c}{H(z)(1+z)}\bar{j}_\nu(z), \tag{13}$$

where the mean comoving emission coefficient $\bar{j}_\nu(z)$ is expressed as:

$$\bar{j}_\nu(z) = \int {\rm d}L \frac{{\rm d}n}{{\rm d}L}(M, z)\frac{L_{\nu(1+z)}}{4\pi}. \tag{14}$$

The term $L_{\nu(1+z)}$ denotes the galaxy infrared luminosity emitted at frequency $\nu(1 + z)$, and ${\rm d}n/{\rm d}L$ is the infrared galaxy luminosity function.

The main feature of the halo model for CIB anisotropies is the description of the galaxy luminosity as a parametric function of frequency, redshift, and halo mass as:

$$L_{(1+z)\nu}(M, z) = L_0\Phi(z)\Sigma(M)\Theta[(1+z)\nu]. \tag{15}$$

The redshift evolution of the infrared luminosity is one of the most uncertain parameters in the model. We assume a power law, dependent on a single parameter δ as:

$$\Phi(z) = (1+z)^\delta. \tag{16}$$

The exact value of this parameter is unknown, especially at redshifts $z \geq 2$, which is particularly relevant for our cross-correlations with quasars. Semi-analytic models and numerical simulations predict different evolutions of the luminosity with redshift (De Lucia & Blaizot 2007; Neistein & Dekel 2008; Oliver et al. 2010; Bouché et al. 2010; Weinmann, Neistein & Dekel 2011; Wu, Doré & Teyssier 2016). For this reason, we will consider δ as a free parameter in our model.

The dependence on the dark matter halo mass is parametrized with a log-normal function as:

$$\Sigma(M) = \frac{M}{M_N}\frac{1}{(2\pi\sigma^2_{L/M})^{0.5}}\exp\left[-\frac{(\log_{10}M - \log_{10}M_{\rm eff})^2}{2\sigma^2_{L/M}}\right]; \tag{17}$$

Downloaded from https://academic.oup.com/mnras/article-abstract/478/2/1911/4995923 by Lawrence Berkeley National Laboratory user on 22 January 2019

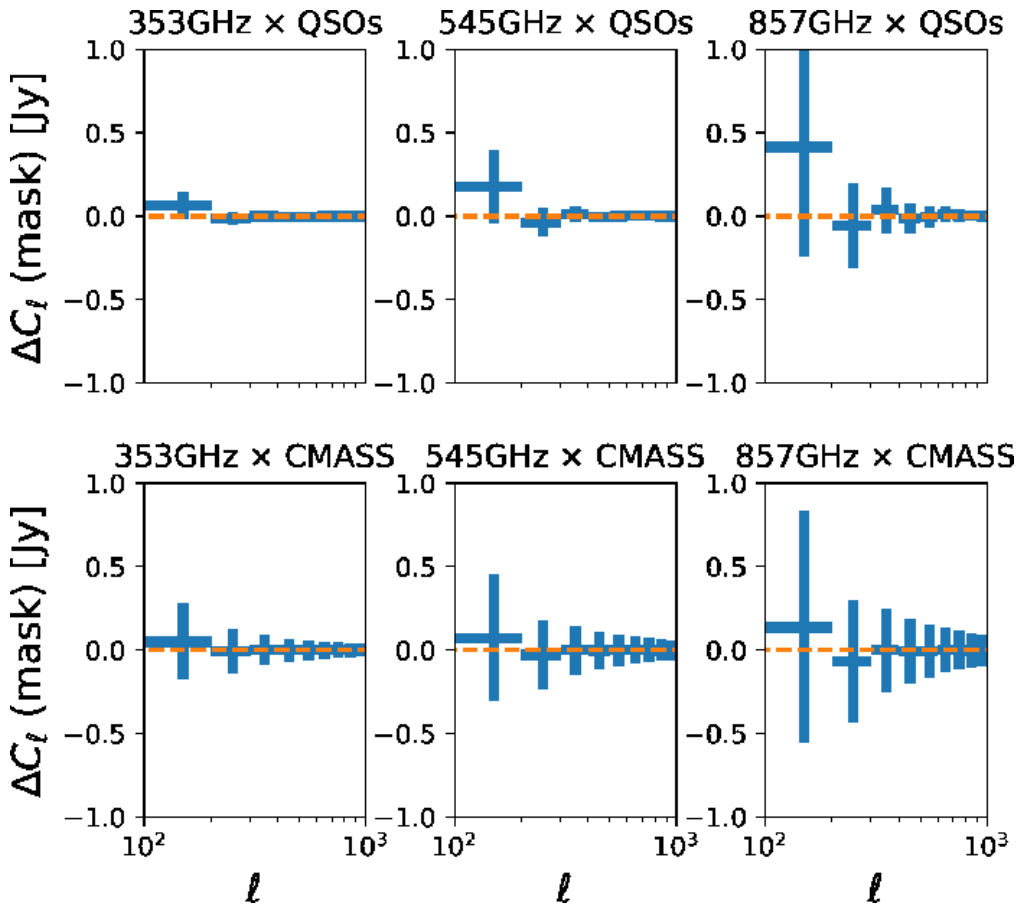

Figure 3. The difference in the angular cross-power spectra between the 40 per cent Galactic dust mask, which we use for our final results, and the 20 per cent Galactic dust mask with 1σ errors. We include difference estimates for the Planck-quasar (top) and Planck-CMASS (bottom) angular cross-power spectra. The differences for all the spectra appear to be consistent with a null result.

where $M_{\rm N}$ is a normalization parameter, while $M_{\rm eff}$ describes the halo mass that is most efficient at hosting star formation. Simulations have shown that various mechanisms prevent an efficient star formation for halo masses much lower and much higher than $M_{\rm eff}$ (Benson et al. 2003; Silk 2003; Bertone, Stoehr & White 2005; Croton et al. 2006; Dekel & Birnboim 2006; Béthermin, Doré & Lagache 2012a; Behroozi, Wechsler & Conroy 2013). We fix the value of this parameter at $\log(M_{\rm eff})[M_{\odot}] = 12.6$, in agreement with Planck Collaboration et al. (2014c) and Serra et al. (2016). The parameter $\sigma_{\rm L/m}$ accounts for the range of halo masses mostly contributing to the infrared luminosity, and has been fixed at $\sigma_{\rm L/m} = 0.5$ (Shang et al. 2012; Planck Collaboration et al. 2014c; Serra et al. 2014, 2016).

A simple functional form (see Blain et al. 2002, and reference therein) is assumed for the galaxy Spectral Energy Distribution (SED):

$$\Theta(\nu) \propto \begin{cases} \nu^{\beta} B_{\nu}(T_{\rm d}) & \nu < \nu_0\,; \\ \nu^{-2} & \nu \geq \nu_0, \end{cases} \tag{18}$$

where $T_{\rm d}$ is the dust temperature averaged over the redshift range considered, and β is the emissivity of the Planck function $B_{\nu}(T_{\rm d})$. We will assume $\beta = 1.5$ in the rest of the analysis, in agreement with Planck Collaboration (2014). A free parameter, $A_{\rm C\,II}$, is included in the fit to quantify the mean amplitude of the CII line. At the C II emission frequency $\nu_{\rm C\,II} = 1901.03$ GHz, we assume that the galaxy SED is the sum of the modified blackbody plus the CII mean line intensity as:

$$\Theta(\nu_{\rm C\,II}) = \Theta(\nu_{\rm C\,II})(1 + A_{\rm C\,II}). \tag{19}$$

Note that this expression assumes that all galaxies that emit CIB will also emit the C II line. This should be a valid assumption since all galaxies should have an ionized phase and a PDR, both of which should produce CII emission. Thus, although the intensity of the C II line should vary from galaxy to galaxy, all galaxies should emit C II. In order to extract the full line information for the C II emission, we could also use the Planck bandpasses as weight functions in the C_{ℓ} model. We leave this for future work.

Finally, we must consider the additional cross-correlation between the Planck 353 GHz map and both QSOs and LRGs, due to the thermal Sunyaev–Zeldovich (tSZ) effect (Sunyaev & Zeldovich 1972). We checked that the contamination is negligible for QSOs, but not for LRGs. We thus added a template describing the CIB×LRGs cross-power spectrum at 353 GHz due to the tSZ effect, scaled with an amplitude $A_{\rm tSZ}$, which is a free parameter in our model. Based on the formalism in Komatsu & Kitayama (1999), we construct the template for the SZ-LSS cross-correlation as

$$C_{\ell}^{\rm LSS-SZ} = \int \frac{{\rm d}z}{\chi^2} \left(\frac{d\chi}{{\rm d}z}\right)^{-1} b_{\rm LSS} \tag{20}$$

$$\frac{{\rm d}n}{{\rm d}z}(z) \left\langle b \frac{{\rm d}y}{{\rm d}z} \right\rangle_{SZ} P_{\rm DM}(k, z), \tag{21}$$

Downloaded from https://academic.oup.com/mnras/article-abstract/478/2/1911/4995923 by Lawrence Berkeley National Laboratory user on 22 January 2019

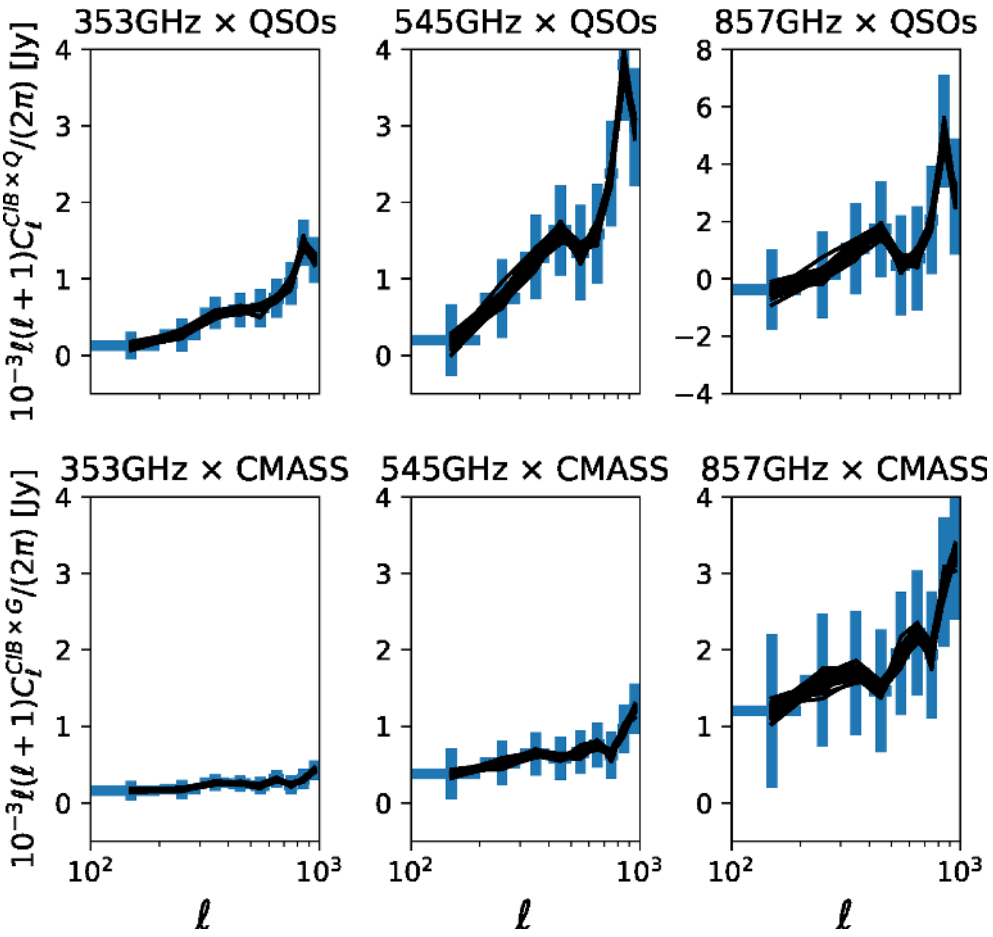

Figure 4. The jackknife test for our Planck-quasar (top) and Planck-CMASS (bottom) angular cross-power spectrum measurements. We construct 40 (37) jackknife regions for the quasars (galaxies), computing estimates of C_ℓ^{T-Q} (C_ℓ^{T-G}), excluding each jackknife region. The black lines are the C_ℓs excluding each jackknife region. These estimates appear to be consistent with the full measurement (blue crosses), suggesting that our measurement is not dominated by foregrounds.

where

$$\left\langle b\frac{\mathrm{d}y}{\mathrm{d}z}\right\rangle_{SZ} = \frac{dV}{dz\,d\Omega}\int dM\, n(M,z)y_\ell(M,z)b(M,z), \tag{22}$$

$n(M, z)$ and $b(M, z)$ are the Tinker halo mass function and halo bias (Tinker et al. 2008), and $y_\ell(M, z)$ is the two-dimensional Fourier transform of the projected Compton-y profile, given in Komatsu & Seljak (2002). We then multiply the template by 1.78×10^9 Jy sr^{-1} to convert the Compton-y parameter to an intensity in the Planck 353 band based on the formula

$$I_\nu^{\mathrm{SZ}} = g(\nu)T_{\mathrm{CMB}}\left(\frac{I_\nu^{SZ}}{T_{\mathrm{CMB}}}\right), \tag{23}$$

where $g(\nu)T_{CMB}$ is the change in the CMB temperature due to the SZ effect, and I_ν/T_{CMB} is the conversion from CMB temperature to intensity, listed in table 1 in Planck Collaboration et al. (2014c). The $C_\ell^{\mathrm{LSS-SZ}}$ template is then added to the $C_\ell^{\mathrm{LSS-T}}$ model in equation (12) when performing the MCMC analysis.

We perform a MCMC exploration of the parameter space with a modified version of the publicly available code `cosmomc` (Lewis & Bridle 2002) and using flat priors on the following set of free parameters:

$$\Xi \equiv \{T_d, \delta, L_0, A_{\mathrm{C\,II}}, A_{\mathrm{tSZ}}, b_{\mathrm{QSO}}\}. \tag{24}$$

For b_{QSO}, we set a prior b_{QSO}= [3.2, 3.8] based on the angular autopower spectrum measurement discussed above. Note that although we expect b_{QSO} to vary across the redshift range, we can treat it as an 'effective bias' for our measurement since we are only searching for a redshift-independent signal, namely the C II amplitude. We were unable to perform a joint fit for b_{QSO} with a broad uniform prior because the CIB redshift evolution parameter δ was too degenerate with b_{QSO} to perform the fit without an independent measurement of δ. We fit nine data points for each cross-power spectrum in the multipole range $100 < l < 1000$ and, in order to obtain stronger constraints on the main CIB parameters, we also fit both the mean level of the CIB at 353, 545, 857 GHz (Béthermin et al. 2012b) and a compilation of 10 star formation rate density (SFRD) measurements presented in Madau & Dickinson (2014) and averaged over the redshift range $0 < z < 4$, as in Serra et al. (2016).

With six free parameters, we are able to obtain a good fit to the data, with a reduced χ^2 equal to $\chi^2/N_{\mathrm{d.o.f.}} = 1.3$. In Fig. 1 we plot the best-fitting curves obtained for the six cross-power spectra used in the analysis. The mean value inferred for the CIB dust temperature is $T_d = 27.2 \pm 0.7$ K, broadly compatible with current measurements, see e.g. Magnelli et al. (2014). The redshift evolution parameter is constrained as $\delta = 2.3 \pm 0.1$, in agreement with constraints from previous analyses of CIB autopower spectra (Viero et al. 2013;

Downloaded from https://academic.oup.com/mnras/article-abstract/478/2/1911/4995923 by Lawrence Berkeley National Laboratory user on 22 January 2019

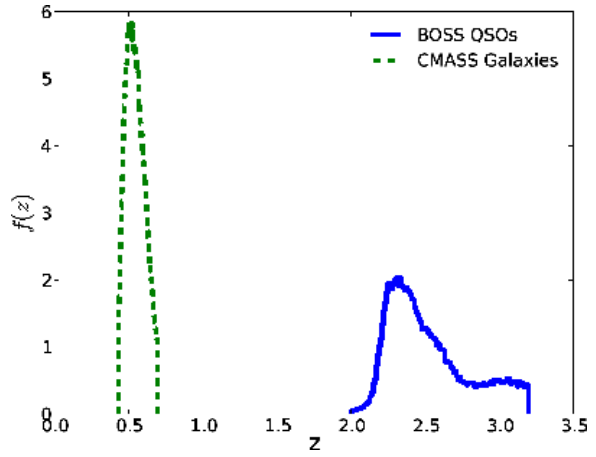

Figure 5. Redshift distributions of the BOSS spectroscopic quasars and CMASS galaxies.

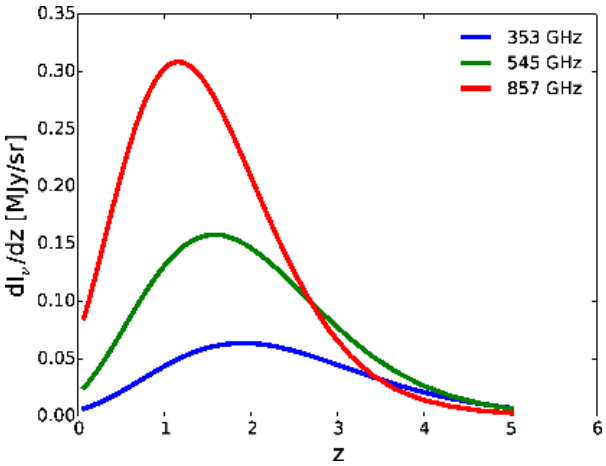

Figure 6. Best-fitting CIB redshift distributions for all three Planck bands. These distributions are consistent with those from Schmidt et al. (2015) while also showing an expected frequency dependence due to the redshifting of CIB galaxies.

Serra et al. 2016), although lower than what was found in Planck Collaboration et al. (2014c). The amplitude of the contamination due to the tSZ effect, quantified by the parameter $A_{\rm tSZ}$, is constrained as $A_{\rm tSZ} = 0.75 \pm 0.27$.

These parameter estimates can be used to find the mean level of CIB in each of the Planck bands. Our best-fitting values for each band are $0.64 {\rm nW\,m^{-2}sr^{-1}}$ (353 GHz), $2.2 {\rm nW\,m^{-2}sr^{-1}}$ (545 GHz), and $5.5 {\rm nW\,m^{-2}sr^{-1}}$ (857 GHz). These values are in good agreement with results from table 10 of Planck Collaboration et al. (2014c) and with results from Béthermin et al. (2012b), which both use autocorrelations in their measurements. An agreement between autocorrelations and cross-correlations for the fits implies that the CIB is well described as being fully correlated with the CMASS galaxy and quasar samples. Since the CII line should also be fully correlated with the CIB, then we can describe the C II emission as being fully correlated with the LSS tracers. If the C II emission and the LSS tracers were not fully correlated, then the C II constraint would be biased downward. Thus, our results allow us to neglect this complication.

In Fig. 6 we plot the redshift distribution of the CIB based on our fit. We find a redshift distribution consistent with that found in

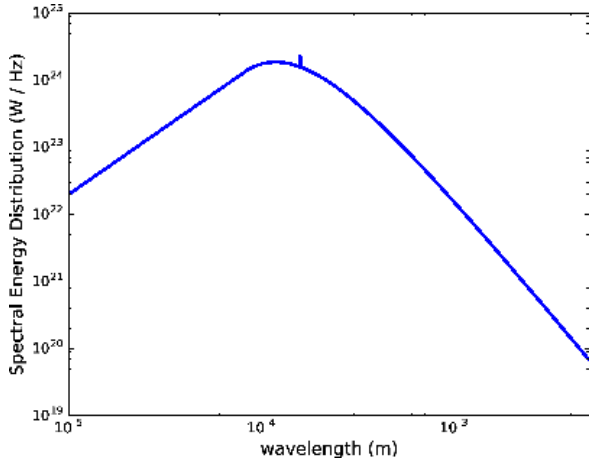

Figure 7. Best-fitting SED for a galaxy at $z \sim 2.49$, where C II emission at 1901 GHz can be detected in cross-correlation between a QSO map and Planck's 545 GHz channel. The SED components include a modified blackbody for the CIB and a C II emission line. The modified blackbody parameters are in agreement with previous CIB measurements (Béthermin et al. 2012b; Planck Collaboration et al. 2014c).

Schmidt et al. (2015) and as shown in their fig. 1. We do see a slight discrepancy in our amplitude for the 857 GHz band distribution is a bit lower than that in Schmidt et al. (2015). Also, we claim the peak positions in our distributions show an expectant frequency dependence due to the fact that higher redshift galaxies should contribute to lower frequency bands, while the distributions in Schmidt et al. (2015) have peaks in the small range of $z \simeq 1.2-1.4$.

Finally, the constraint on the C II amplitude is set as $A_{\rm C\,II} = 0.56^{+0.42}_{-0.40}$ at 95 per cent confidence level, which implies a mean intensity of the CII line as: $I_{\rm C\,II} = 6.6^{+5.0}_{-4.8} \times 10^4\,{\rm Jy\,sr^{-1}}$ (95 per cent confidence level). In Fig. 7 we present the best-fitting galaxy SED with a CII line, and in Fig. 8 we show the two-dimensional contour regions for the main parameters of the model. Remember that we also perform this MCMC removing the three highest ℓ-bins ($\ell > 700$) of the three Planck-galaxy C_ℓs to test for bias due to non-linear clustering. This result is unchanged relative to the fit using all the ℓ-bins.

5.2 Contaminating spectral lines

C II is not the only emission line that could be present in the Planck maps. All three Planck bands we use in our fit should be contaminated by lines other than CII and many of them should appear at the right redshifts to correlate with either the BOSS quasars or the CMASS galaxies, biasing our CIB and C II measurements. The major ones include O I (145 μm) and O III (88 μm) for the correlations with BOSS quasars and N II (205 μm) for the correlations with the CMASS galaxies, although much of the signal also comes from fainter lines.

To estimate how biased are our CIB and C II estimates, we compute the angular cross-power spectra with all the lines from table 1 of Visbal, Trac & Loeb (2011) included to see how much the amplitudes of the spectra are affected. We use the best-fitting value for $A_{\rm C\,II}$ to compute the C II contribution, and then scale the contributions from the other lines based on their listed luminosity-to-star-formation ratios *L*/*SFR* in Visbal et al. (2011). Specifically, the SED

Downloaded from https://academic.oup.com/mnras/article-abstract/478/2/1911/4995923 by Lawrence Berkeley National Laboratory user on 22 January 2019

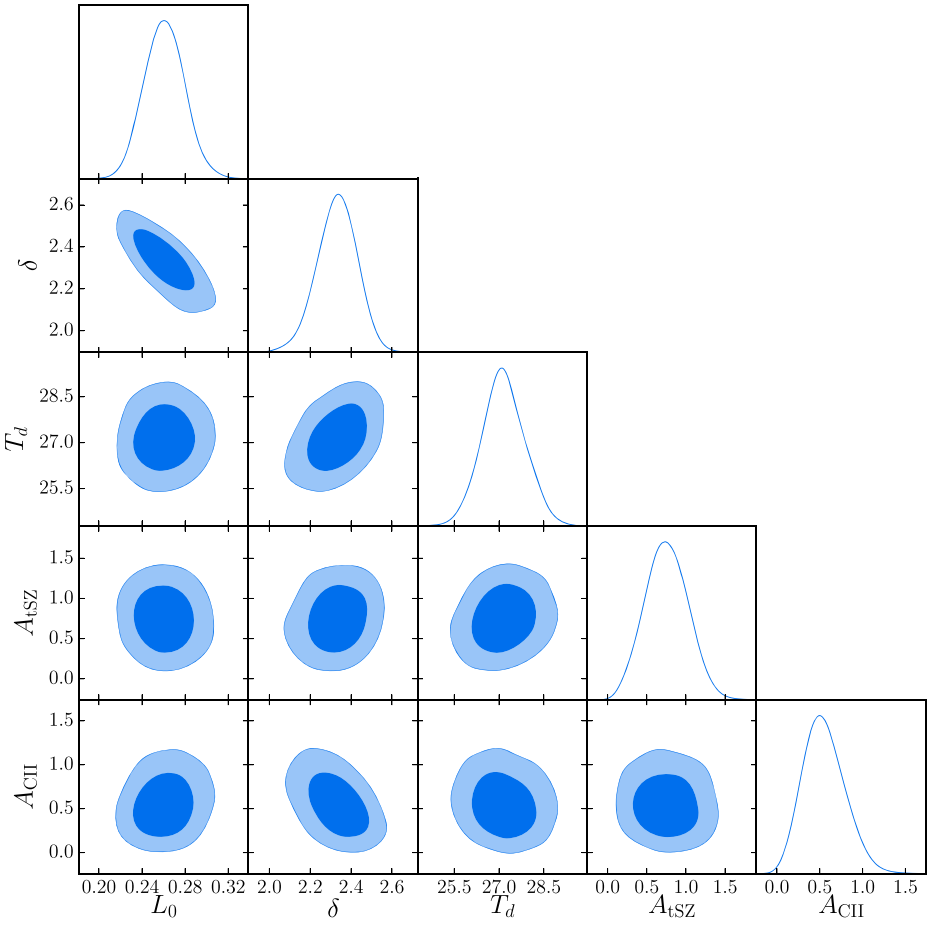

Figure 8. Triangle panel showing two-dimensional confidence regions at 68 per cent and 95 per cent for the main parameters of the model.

$\Delta\Theta$ added to the clean SED Θ at the rest frequency of line X (ν_X) is

$$\Delta\Theta(\nu_X) = A_{\rm C\,II}\Theta(\nu_{\rm C\,II})\left(\frac{(L/SFR)_X}{(L/SFR)_{\rm C\,II}}\right). \quad (25)$$

This is used to calculate the total C_ℓ^{T-LSS} in equation (12) including all the lines. We then subtract C_ℓ^{T-LSS} without interlopers to get the interloper contribution, ΔC_ℓ^{T-LSS}. Note that we do not consider distortions due to projection effects (Lidz & Taylor 2016) because C_ℓ is already projected along the line of sight, such that even upon a shift in redshift, fluctuations per pixel are conserved.

In Fig. 9 we plot all six cross-correlations, including both C_ℓ^{T-LSS} (no interlopers) and ΔC_ℓ^{T-LSS}. We plot C_ℓ^{CII-Q} (no interlopers) and ΔC_ℓ^{CII-Q} in Fig. 10. We can see that the interloper contribution to the total C_ℓ^{T-LSS} is indeed subdominant. The results for all six cross-correlations, plus the CII-quasar cross-correlation, are listed in Table 1. We find that most of the correlations change by less than two per cent when including the interlopers, while C_ℓ^{353-G} increases by 2.3 per cent and $C_\ell^{\rm C\,II-Q}$ increases by 2.5 per cent. Thus, we expect that the CIB and C II measurements are biased by less than three per cent, which is significantly less than our measurement errors. We do caution, however, that the line ratios used were measured using low-redshift galaxies and may not be fully accurate. It should also be noted that the luminosity-to-star-formation ratios in Visbal et al. (2011) were calculated using different sets of galaxies, so there also could be miscalibrations. We do not expect the line intensities to possibly be of high significance for our measurements, so we do not consider it further.

6 DISCUSSION

Our analysis implies a non-zero amplitude of the mean C II emission line at more than 95 per cent confidence level. Taken at face value, this would be the first measurement of the C II line from Planck's temperature maps. Because the model used to fit the data is quite uncertain (especially in the redshift range relevant for the cross-correlation between temperature maps and quasars), it is interesting to ask whether such a detection is real or due to our ignorance of the exact values of some key parameters. In the context of Bayesian model selection, it is possible to assess the need to include the CII amplitude in the fit by computing the Bayesian evidence ratio, or Bayes Factor B (Heavens 2009), using the best-fitting likelihood values obtained from the MCMC fits to the data with and without a free CII amplitude. We compute B as the evidence for the non-C II model versus the C II model. Using the Laplace approximation, the expression for the Bayes Factor in this case is given by

$$B = \sqrt{\frac{\det \mathbf{C}'}{2\pi \det \mathbf{C}}}\exp\left(-\frac{1}{2}\delta\theta_\alpha[\mathbf{C}^{-1}]_{\alpha\beta}\delta\theta_\beta\right)\Delta A_{\rm C\,II}, \quad (26)$$

where θ_α label the six parameters in the MCMC fit including $A_{\rm C\,II}$, $\delta\theta_\alpha$ are the differences between the best-fitting parameter values among the two MCMC fits, $\Delta A_{\rm C\,II} = 10$ is the prior on $A_{\rm C\,II}$, and $\mathbf{C}$ and $\mathbf{C}'$ are the covariance matrices for the parameters for the MCMC fit with and without a free $A_{\rm C\,II}$, respectively. Note that in the fit without C II emission, $A_{\rm C\,II} = 0$ such that $\delta\theta(A_{\rm C\,II}) = A_{\rm C\,II}$. We evaluate a value for the Bayes Factor of B= 1.48 that slightly

Downloaded from https://academic.oup.com/mnras/article-abstract/478/2/1911/4995923 by Lawrence Berkeley National Laboratory user on 22 January 2019

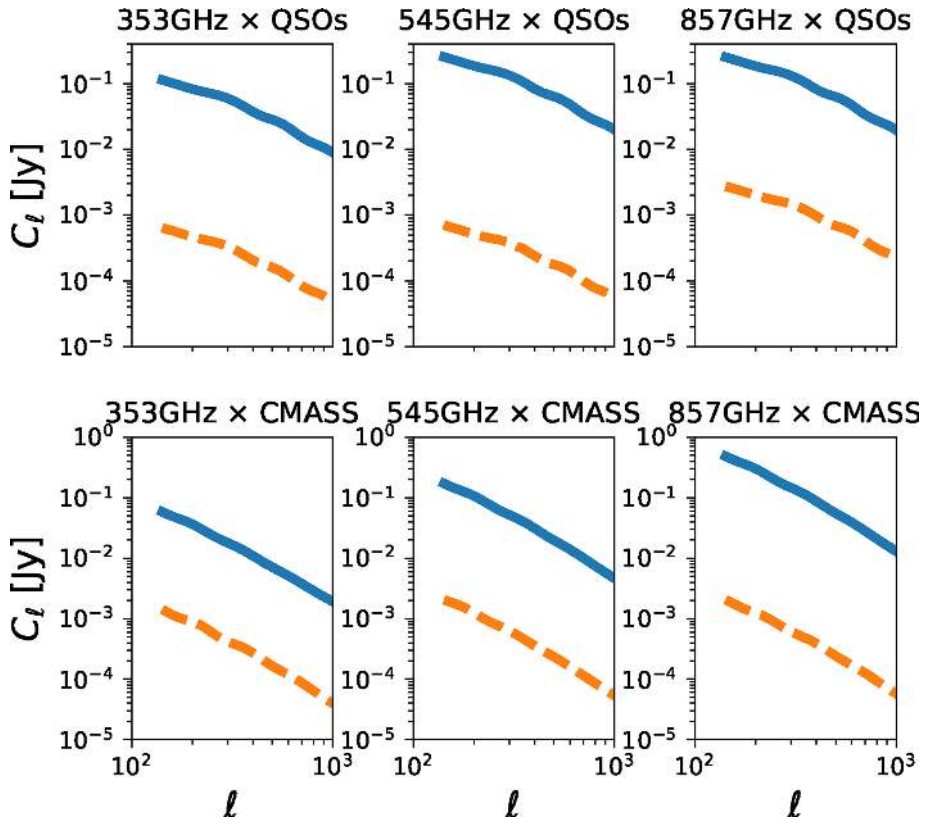

Figure 9. The contribution of interlopers to the measured angular cross-power spectra. We plot C_ℓ^{T-LSS} (solid) and ΔC_ℓ^{T-LSS} (dashed) for all six cross-correlations. We see that the interlopers contribute negligibly to the power spectra compared to our measurement errors.

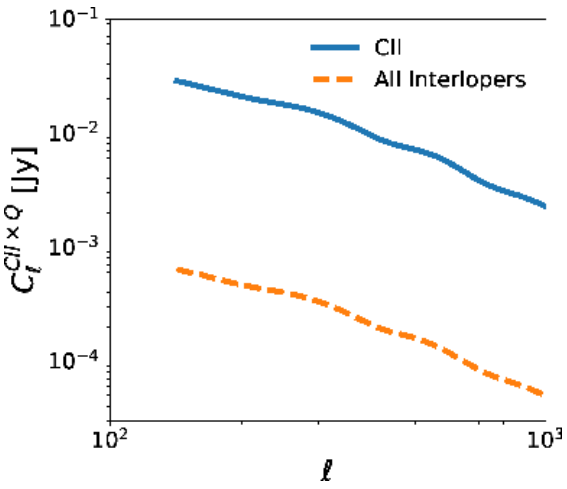

Figure 10. The contribution of interlopers to the constructed angular C II QSO cross-power spectrum. We plot $C_\ell^{\mathrm{C\,II}Q}$ (solid) and $\Delta C_\ell^{\mathrm{C\,II}Q}$ (dashed) for all six cross-correlations. We see that the interlopers contribute negligibly to the power spectra compared to our measurement errors.

favors the model without CII emission, but the rule-of-thumb is that a result $B \lesssim 3$ is inconclusive. We thus see that the data are not discriminative enough to allow an assessment of the need for the CII parameters in the fit. More sensitive measurements will be needed in the future to discriminate between the C II and non-CII models.

Although we cannot assert a detection of C II emission, we can place constraints on C II models under the assumption that the C II emission does exist. We consider several models in relation to our constraints. The first model (Gong12) uses the values from Gong et al. (2012), which predicts the C II intensity from collisional excitation models as a function of the kinetic temperature and number densities of electrons, T_k^e and n_e, respectively. We also include a modified version of Gong12 where (1) we change the cosmological parameters to match those from joint *Planck*-BOSS constraints (Planck Collaboration et al. 2014b; Alam et al. 2016) and (2) we replace the quantity $f_{\mathrm{gas}}^{\mathrm{cr}} \overline{n}_b(z)$ in the Gong12 model, where $f_{\mathrm{gas}}^{\mathrm{cr}}$ is the fraction of gas in collapsed haloes and $\overline{n}_b(z)$ is the average number

Table 1. Bias to Planck-LSS cross-power amplitudes due to interloping spectral lines, as well as the bias to the C II quasar cross-correlation. The values were derived using luminosity-to-star-formation ratios from table 1 of Visbal et al. (2011). The luminosity-to-star-formation ratios mostly come from calculations by Righi et al. (2008) using low-redshift galaxies (Malhotra et al. 2001) and measurements of the galaxy M82 (Panuzzo et al. 2010). These biases are insignificant relative to our errors.

C_ℓ	Interlopers	$\Delta C_\ell / C_\ell$ [per cent]
353-QSO	^{12}CO(10-9),^{12}CO(11-10), ^{12}CO(12-11)	0.55
545-QSO	OI	0.28
857-QSO	OIII	1.1
353-CMASS	^{12}CO(5-4),^{13}CO(5-4),HCN(6-5)	2.3
545-CMASS	^{12}CO(7-6),^{12}CO(8-7),CI, ^{13}CO(7-6),^{13}CO(8-7)	1.2
857-CMASS	^{12}CO(11-10),^{12}CO(12-11),NII	0.44
C II-QSO	all interlopers	2.5

Downloaded from https://academic.oup.com/mnras/article-abstract/478/2/1911/4995923 by Lawrence Berkeley National Laboratory user on 22 January 2019

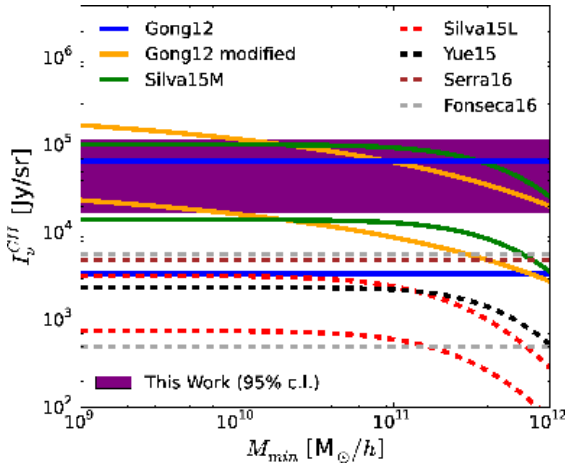

Figure 11. Measurement of the quantity C II intensity with 95 per cent confidence limits. We also show the range of predictions for several C II intensity models, including collisional excitation models (solid lines) and scaling relations (dashed lines), as functions of minimum halo mass $M_{\rm min}$ (see text for details). Our measurement favors the collisional excitation models that appear at the high end of the range of models, although no models are ruled out by 3σ.

density of baryons, with

$$f_{\rm gas}^{\rm cr}\bar{n}_b(z) = \frac{\Omega_b}{\Omega_m}\frac{1-Y_{\rm He}}{m_p}\rho_{\rm halo}(z), \quad (27)$$

where Ω_b and Ω_m are the relative baryon and matter cosmological densities, respectively, $Y_{\rm He}$ is the helium mass fraction, and m_p is the proton mass. We then consider two models from Silva et al. (2015). One model (S15M) updates the Gong12 model with recent metallicity simulations (De Lucia & Blaizot 2007; Guo et al. 2011). The other model (Silva15L) uses various low-redshift luminosity measurements to construct a $L_{\rm C\,II} - \psi$ relation, where ψ is the star formation rate, with the star formation rate constructed using the previously mentioned simulations (De Lucia & Blaizot 2007; Guo et al. 2011). For models Gong12 and Silva15M the range shown is somewhat based on the range of T_k^e and n_e values considered in Gong et al. (2012). While the lower range corresponds to $T_k^e = 10^2$ K and $n_e = 1$ cm^{-3}, the upper range corresponds to the highest possible value allowed in the model, where $T_k^e = n_e \to \infty$ sets an infinite spin temperature for the C II transition. Next, we consider a C II emission model by Yue et al. (2015), which we call Yue15. This model constructs a $L_{\rm C\,II}(\psi, Z)$ fitting formula, where Z is the galaxy metallicity. The metallicity model used is dependent on the stellar mass within the halo, which we attain for the haloes using results from Behroozi et al. (2013). We also consider a model (Serra16) given in Serra et al. (2016). We can separate these models into two sets: the Gong12 and Silva15M models are collisional excitation models where the CII intensity is produced by collisional excitations of C II ions and electrons, and the other models are scaling relations where the C II intensity is modelled based on measured luminosity functions or SFRD measurements at low redshifts. Note that the range of the models given in Fonseca et al. (2017) comprises the predictions of the scaling relation models. The collisional excitation models tend make higher predictions than the scaling relation models. Of course, changes in other model and clustering parameters can change the predictions.

In Fig. 11, we show our C II intensity constraints along with predictions based on these seven models for CII emission. We find that our constraints favour the collisional excitation models, although none of the models shown are ruled out, in that our $A_{\rm C\,II}$ measurement is not 3σ away from zero. In addition, more measurements need to be performed to rule out any foreground contamination that could bias our results. Note that the Gong12 model assumes that the ground state fraction of CII ions is one-third for all CII spin temperatures, which is actually not valid at the low-intensity end when the spin temperature is much less than the CMB temperature. This is why the spread in the Gong12 model is much larger than that of the modified Gong12 and Silva15M models where we use the spin-temperature-dependent ground fraction. These two models are well within our constraints for reasonable values of T_k^e and n_e, although our constraints favour $M_{\rm min} < 10^{11} M_\odot\, h^{-1}$ for C II emission. These models are subject to improvement as we get more higher redshift measurements of CII luminosities.

6.1 Forecasts for upcoming surveys

Looking forward, we consider how sensitive upcoming surveys could be to C II emission using cross-correlations. First, we replace BOSS spectroscopic quasars with quasars from the upcoming DESI (Levi et al. 2013). In the redshift range $z = 2-3.2$, DESI will observe six times more quasars than the BOSS sample we used in our analysis. We also assume that we will use the DESI LRG sample to help constrain the CIB emission. We assume that dust and CMB emission, as in our measurement, will not be subtracted from the Planck maps.

To forecast the C II sensitivity, we perform a Fisher calculation of the errors over six cross-correlations between the three Planck bands and the DESI LRGs and quasars, assuming the best-fitting values from our measurement. We first confirm that we could reproduce the sensitivity of our current measurement with a Fisher analysis, and we find that our Fisher errors are close to those found from the MCMC. The Fisher error for the CII intensity is about 1.3 times the MCMC error, which is reasonable. We predict the SNR of the CII intensity for the Planck/DESI configuration to be 10, or approximately five times greater than that from our measurement. This type of measurement would be able to confirm or rule out our CII measurement.

In addition, we consider detecting C II emission in the proposed PIXIE (Kogut et al. 2011; Switzer 2017) by cross-correlating its intensity maps with maps of LRGs and quasars from the upcoming DESI (Levi et al. 2013). For PIXIE, we assume the specifications given in Hill et al. (2015), and we also assume that the DESI footprint is totally contained within the PIXIE footprint. The PIXIE spectrometer has much higher spectral resolution because of Planck, with bandwidths of 15 GHz over the range of 30–1230 GHz. Because of this, we assume that dust and the CMB could be subtracted directly from the maps, allowing us to remove them from the statistical noise. In order to do a straightforward comparison with our measurement, we group the relevant channels into the 353, 545, and 857 GHz bands from Planck and increase the band sensitivities by $\sqrt{N_{\rm channel}}$, while also considering a real number densities of LRGs and quasars over the same redshift ranges as we used for the CMASS galaxies and BOSS quasars in our measurement. Also, PIXIE has a angular beam size of 1.6°, much larger than Planck, so we only consider modes $100 < \ell < 512$.

We also perform a Fisher calculation of the errors over six cross-correlations, this time between the three (simulated) bands using PIXIE channels and the DESI LRGs and quasars, assuming the best-fitting values from our measurement. Note that we set up our forecasts to comprise the same redshift range as our measurement, though we consider a subset of the comoving scales. We find that

Downloaded from https://academic.oup.com/mnras/article-abstract/478/2/1911/4995923 by Lawrence Berkeley National Laboratory user on 22 January 2019

the sensitivity of the PIXIE/DESI configuration is 26, or ∼13 times greater than that from our measurement. In addition, the high spectral resolution of PIXIE should make it better equipped to remove interlopers by cross-correlating the LRG and quasar samples with individual PIXIE channels. Assuming a CII intensity the same as our measurement, this should be strong enough to make relevant constraints on the kinetic temperature and number density of electrons in the PDRs powering the CII emission. Also, a C II intensity of the measured magnitude extrapolated to $z \simeq 6$ based on the Gong12 model could have an intensity approximately equal to those in the forecasts for TIME-Pilot (Crites et al. 2014), which predicted an SNR of ≃7. Although the SNR may vary from this value due to uncertainties in the redshift evolution over this range, we should still learn more about the physical processes behind CII emission through these measurements.

7 CONCLUSIONS

We place the first constraints on C II emission at large scales and redshifts $z = 2-3$ using cross-power spectra between high-frequency Planck intensity maps and both spectroscopic quasars and CMASS galaxies from SDSS-III. We find $I_{\rm C\,II} = 6.6^{+5.0}_{-4.8} \times 10^4$ Jy sr^{-1} (95 per cent confidence level), which favors collisional excitation models, such as the Gong12 (Gong et al. 2012) and Silva15M (Silva et al. 2015) models over models from luminosity scaling relations, though neither are ruled out. In addition, lower values for the minimum CII -emitting haloes are also favoured, specifically $M_{\rm min} < 10^{11} {\rm M}_\odot\,{\rm h}^{-1}$. We found that the contribution from interloping lines are small compared to measurement errors. The non-CII model is equally plausible based on the data, and if confirmed through more sensitive measurements, this emission could also be (partially) due to other lines, or some unknown systematic. More sensitive measurements are needed to confirm this extragalactic signal and rule out foreground contamination, which could be forthcoming using upcoming galaxy surveys such as DESI with Planck or the potential sky survey PIXIE. If this C II measurement is confirmed, it will open up a new window into large-scale structure, even up through the epoch of reionization.

ACKNOWLEDGEMENTS

We thank J. Aguirre, A. Lidz, and A. Myers for helpful comments. AP was supported by a McWilliams Fellowship of the Bruce and Astrid McWilliams Center for Cosmology. SH is supported by DOE and NSF AST1412966.

Part of the research described in this paper was carried out at the Jet Propulsion Laboratory, California Institute of Technology, under a contract with the National Aeronautics and Space Administration.

This work is based on observations obtained with *Planck* (http://www.esa.int/Planck), an ESA science mission with instruments and contributions directly funded by ESA Member States, NASA, and Canada.

Funding for SDSS-III has been provided by the Alfred P. Sloan Foundation, the Participating Institutions, the National Science Foundation, and the U.S. Department of Energy Office of Science. The SDSS-III web site is http://www.sdss3.org/.

SDSS-III is managed by the Astrophysical Research Consortium for the Participating Institutions of the SDSS-III Collaboration including the University of Arizona, the Brazilian Participation Group, Brookhaven National Laboratory, Carnegie Mellon University, University of Florida, the French Participation Group, the German Participation Group, Harvard University, the Instituto de Astrofisica de Canarias, the Michigan State/Notre Dame/JINA Participation Group, Johns Hopkins University, Lawrence Berkeley National Laboratory, Max Planck Institute for Astrophysics, Max Planck Institute for Extraterrestrial Physics, New Mexico State University, New York University, Ohio State University, Pennsylvania State University, University of Portsmouth, Princeton University, the Spanish Participation Group, University of Tokyo, University of Utah, Vanderbilt University, University of Virginia, University of Washington, and Yale University.

REFERENCES

Aihara H. et al., 2011, ApJS, 193, 29
Alam S., Zhu H., Croft R. A. C., Ho S., Giusarma E., Schneider D. P., 2017, MNRAS, 470, 2822
Alam S. et al., 2015, ApJS, 219, 12
Alam S. et al., 2016, MNRAS, 470, 2617
Anderson L. et al., 2014, MNRAS, 441, 24
Bandura K. et al., 2014, in Stepp L., Gilmozzi R., Hall H., eds, Proc. SPIE Conf. Ser, 9145, p. 914522
Basu K., Hernández-Monteagudo C., Sunyaev R. A., 2004, A&A, 416, 447
Behroozi P. S., Wechsler R. H., Conroy C., 2013, ApJ, 770, 57
Benson A. J., Bower R. G., Frenk C. S., Lacey C. G., Baugh C. M., Cole S., 2003, ApJ, 599, 38
Bersanelli M. et al., 2010, A&A, 520, A4
Bertone S., Stoehr F., White S. D. M., 2005, MNRAS, 359, 1201
Blain A. W., Smail I., Ivison R. J., Kneib J.-P., Frayer D. T., 2002, Phys. Rep., 369, 111
Blanton M. R., Lin H., Lupton R. H., Maley F. M., Young N., Zehavi I., Loveday J., 2003, AJ, 125, 2276
Bouché N. et al., 2010, ApJ, 718, 1001
Bouwens R. J. et al., 2015, ApJ, 803, 34
Bovy J. et al., 2011, ApJ, 729, 141
Breysse P. C., Kovetz E. D., Kamionkowski M., 2014, MNRAS, 443, 3506
Brown M. L., Castro P. G., Taylor A. N., 2005, MNRAS, 360, 1262
Béthermin M., Doré O., Lagache G., 2012a, A&A, 537, L5
Béthermin M. et al., 2012b, A&A, 542, A58
Carilli C. L., 2011, ApJ, 730, L30
Chang T.-C., Pen U.-L., Bandura K., Peterson J. B., 2010, Nature, 466, 463
Chang T.-C., Pen U.-L., Peterson J. B., McDonald P., 2008, Phys. Rev. Lett., 100, 091303
Chang T. C., Gong Y., Santos M., Silva M. B., Aguirre J., Doré O., Pritchard J., 2015, Advancing Astrophysics with the Square Kilometre Array (AASKA14), p. 4
Cheng Y.-T., Chang T.-C., Bock J., Bradford C. M., Cooray A., 2016, ApJ, 832, 165
Comaschi P., Ferrara A., 2016, MNRAS, 455, 725
Cooray A. et al., 2016, preprint (arXiv:1602.05178)
Crites A. T., et al., 2014, in Holland W., Zmuidzinas J., eds, Proc. SPIE Conf. Ser., 9153, Bellingham, p. 91531W
Croton D. J. et al., 2006, MNRAS, 365, 11
Dawson K. S. et al., 2013, AJ, 145, 10
DeBoer D. R. et al., 2017, PASP, 129, 045001
Dekel A., Birnboim Y., 2006, MNRAS, 368, 2
De Lucia G., Blaizot J., 2007, MNRAS, 375, 2
Doi M. et al., 2010, AJ, 139, 1628
Doré O. et al., 2014, preprint (arXiv:1412.4872)
Eftekharzadeh S. et al., 2015, MNRAS, 453, 2779
Eisenstein D. J. et al., 2001, AJ, 122, 2267
Eisenstein D. J. et al., 2011, AJ, 142, 72
Fonseca J., Silva M. B., Santos M. G., Cooray A., 2017, MNRAS, 464, 1948
Fukugita M., Ichikawa T., Gunn J. E., Doi M., Shimasaku K., Schneider D. P., 1996, AJ, 111, 1748
Gong Y., Cooray A., Silva M., Santos M. G., Bock J., Bradford C. M., Zemcov M., 2012, ApJ, 745, 49
Gong Y., Cooray A., Silva M. B., Zemcov M., Feng C., Santos M. G., Dore O., Chen X., 2017, ApJ, 835, 273

Downloaded from https://academic.oup.com/mnras/article-abstract/478/2/1911/4995923 by Lawrence Berkeley National Laboratory user on 22 January 2019

Gong Y., Silva M., Cooray A., Santos M. G., 2014, ApJ, 785, 72
Gunn J. E. et al., 1998, AJ, 116, 3040
Gunn J. E. et al., 2006, AJ, 131, 2332
Guo Q. et al., 2011, MNRAS, 413, 101
Górski K. M., Hivon E., Banday A. J., Wandelt B. D., Hansen F. K., Reinecke M., Bartelmann M., 2005, ApJ, 622, 759
Heavens A., 2009, preprint (arXiv:0906.0664)
Hill G. J. et al., 2008, in Kodama T., Yamada T., Aoki K., eds, ASP Conf. Ser., 399, San Francisco, p.115
Hill J. C., Battaglia N., Chluba J., Ferraro S., Schaan E., Spergel D. N., 2015, Phys. Rev. Lett., 115, 261301
Hirata C. M., Padmanabhan N., Seljak U., Schlegel D., Brinkmann J., 2004, Phys. Rev. D, 70, 103501
Hivon E., Górski K. M., Netterfield C. B., Crill B. P., Prunet S., Hansen F., 2002, ApJ, 567, 2
Keating G. K., Marrone D. P., Bower G. C., Leitch E., Carlstrom J. E., DeBoer D. R., 2016, ApJ, 830, 34
Kogut A. et al., 2011, J. Cosmology Astropart. Phys., 7, 25
Komatsu E., Kitayama T., 1999, ApJ, 526, L1
Komatsu E., Seljak U., 2002, MNRAS, 336, 1256
Lamarre J.-M. et al., 2010, A&A, 520, A9
Levi M. et al., 2013, preprint (arXiv:1308.0847)
Lewis A., Bridle S., 2002, Phys. Rev. D, 66, 103511
Lewis A., Challinor A., Lasenby A., 2000, ApJ, 538, 473
Lidz A., Furlanetto S. R., Oh S. P., Aguirre J., Chang T.-C., Doré O., Pritchard J. R., 2011, ApJ, 741, 70
Lidz A., Taylor J., 2016, ApJ, 825, 143
Li T. Y., Wechsler R. H., Devaraj K., Church S. E., 2016, ApJ, 817, 169
Lupton R., Gunn J. E., Ivezić Z., Knapp G. R., Kent S., 2001, in Harnden F. R., Jr, Primini F. A., Payne H. E., eds, ASP Conf. Ser., 238, San Francisco, p. 269
Madau P., Dickinson M., 2014, ARA&A, 52, 415
Madau P., Meiksin A., Rees M. J., 1997, ApJ, 475, 429
Magnelli B. et al., 2014, A&A, 561, A86
Maiolino R. et al., 2015, MNRAS, 452, 54
Malhotra S. et al., 2001, ApJ, 561, 766
Mashian N., Sternberg A., Loeb A., 2015, J. Cosmology Astropart. Phys., 11, 028
Masui K. W. et al., 2013, ApJ, 763, L20
Mennella A. et al., 2011, A&A, 536, A3
Myers A. D. et al., 2015, ApJS, 221, 27
Neistein E., Dekel A., 2008, MNRAS, 383, 615
Oliver S. et al., 2010, MNRAS, 405, 2279
Padmanabhan N. et al., 2008, ApJ, 674, 1217
Panuzzo P. et al., 2010, A&A, 518, L37
Pier J. R., Munn J. A., Hindsley R. B., Hennessy G. S., Kent S. M., Lupton R. H., Ivezić Ž., 2003, AJ, 125, 1559
Planck Collaboration, 2014, A&A, 566, A55
Planck Collaboration et al., 2014a, A&A, 571, A11
Planck Collaboration et al., 2014c, A&A, 571, A30
Planck Collaboration et al., 2016, A&A, 594, A13
Planck et al., 2014b, A&A, 571, A16
Planck HFI Core Team et al., 2011, A&A, 536, A6
Pullen A. R., Chang T.-C., Doré O., Lidz A., 2013, ApJ, 768, 15
Pullen A. R., Doré O., Bock J., 2014, ApJ, 786, 111
Pullen A. R., Hirata C. M., 2013, PASP, 125, 705
Pâris I. et al., 2014, A&A, 563, A54
Reid B. et al., 2016, MNRAS, 455, 1553
Richards G. T. et al., 2002, AJ, 123, 2945
Righi M., Hernández-Monteagudo C., Sunyaev R. A., 2008, A&A, 489, 489
Ross N. P. et al., 2012, ApJS, 199, 3
Sachs R. K., Wolfe A. M., 1967, ApJ, 147, 73
Santos M. et al., 2015, Advancing Astrophysics with the Square Kilometre Array (AASKA14), p. 19
Schmidt S. J., Ménard B., Scranton R., Morrison C. B., Rahman M., Hopkins A. M., 2015, MNRAS, 446, 2696
Scott D., Rees M. J., 1990, MNRAS, 247, 510
Serra P., Doré O., Lagache G., 2016, ApJ, 833, 153
Serra P., Lagache G., Doré O., Pullen A., White M., 2014, A&A, 570, A98
Shang C., Haiman Z., Knox L., Oh S. P., 2012, MNRAS, 421, 2832
Silk J., 2003, MNRAS, 343, 249
Silva M., Santos M. G., Cooray A., Gong Y., 2015, ApJ, 806, 209
Silva M., Santos M. G., Gong Y., Cooray A., Bock J., 2013, ApJ, 763, 132
Silva M., Zaroubi S., Kooistra R., Cooray A., 2017, preprint (arXiv:1711.09902)
Smee S. A. et al., 2013, AJ, 146, 32
Smith J. A. et al., 2002, AJ, 123, 2121
Strauss M. A. et al., 2002, AJ, 124, 1810
Suginohara M., Suginohara T., Spergel D. N., 1999, ApJ, 512, 547
Sunyaev R. A., Zeldovich Y. B., 1972, Comments Astrophys. Space Phys., 4, 173
Switzer E. R., 2017, ApJ, 838, 82
Tinker J., Kravtsov A. V., Klypin A., Abazajian K., Warren M., Yepes G., Gottlöber S., Holz D. E., 2008, ApJ, 688, 709
Tristram M., Macías-Pérez J. F., Renault C., Santos D., 2005, MNRAS, 358, 833
Viero M. P. et al., 2013, ApJ, 772, 77
Visbal E., Loeb A., 2010, J. Cosmology Astropart. Phys., 11, 16
Visbal E., Trac H., Loeb A., 2011, J. Cosmology Astropart. Phys., 8, 010
Weinmann S. M., Neistein E., Dekel A., 2011, MNRAS, 417, 2737
White M. et al., 2011, ApJ, 728, 126
White M. et al., 2012, MNRAS, 424, 933
Wu H.-Y., Doré O., Teyssier R., Serra P., 2016, MNRAS, 375, 3974
Wyithe J. S. B., Loeb A., Geil P. M., 2008, MNRAS, 383, 1195
York D. G. et al., 2000, AJ, 120, 1579
Yue B., Ferrara A., Pallottini A., Gallerani S., Vallini L., 2015, MNRAS, 450, 3829

This paper has been typeset from a TEX/LATEX file prepared by the author.

Downloaded from https://academic.oup.com/mnras/article-abstract/478/2/1911/4995923 by Lawrence Berkeley National Laboratory user on 22 January 2019